

Limits on Dark Matter Compact Objects implied by Supermagnified Stars in Lensing Clusters

Claudi Vall Müller¹, Jordi Miralda-Escudé^{1,2,3}★.

¹*Institut del Ciències del Cosmos, Universitat de Barcelona, Barcelona, Spain*

²*Institució Catalana de Recerca i Estudis Avançats, Barcelona, Spain*

³*Institut d'Estudis Espacials de Catalunya, Barcelona, Spain*

Accepted XXX. Received YYY; in original form ZZZ

ABSTRACT

Supermagnified stars are gravitationally lensed individual stars that are located close to a caustic of a lensing galaxy cluster, and have their flux magnified by a large enough factor (typically ~ 1000) to make them detectable with present telescopes. The maximum magnification is limited by microlensing caused by intracluster stars or other compact objects, which create a network of corrugated critical lines with an angular width proportional to the surface density of microlenses. We consider a set of 9 cases of supermagnified stars reported in the literature, and derive an upper limit on the surface density of compact objects, such as primordial black holes, that might be present as a fraction of the dark matter in addition to known intracluster stars. Any such additional compact objects would widen the corrugated critical line network and therefore the width of the distribution of supermagnified stars around the modeled critical lines of the lens. We find that any compact objects, including primordial black holes, with masses above $\sim 10^{-6} M_{\odot}$ (for which the microcaustics are smaller than the typical angular size of supermagnified stars) cannot account for more than $\sim 3\%$ of the dark matter.

Key words: cosmology – gravitational lensing – dark matter – primordial black holes

1 INTRODUCTION

Several independent observations have demonstrated beyond reasonable doubt that the known baryonic matter accounts for only $\sim 15\%$ of the matter in the Universe, and the remaining 85% is a form of collisionless matter, designated as dark matter since the early work of Zwicky (1933) on galaxy clusters. The first clear evidence for dark matter initially came from galaxy rotation curves and galaxy velocities within groups (Ostriker et al. 1974; Einasto et al. 1974; Rubin et al. 1978), but present evidence has confirmed the existence of cold dark matter (meaning collisionless matter with no appreciable initial velocity dispersion; see Peebles 1982) from a wide variety of other independent observations: the Cosmic Microwave Background fluctuations, which can be explained only with this ratio of baryonic to dark matter (Planck Collaboration et al. 2020; Madhavacheril et al. 2023; Tristram et al. 2024); lensing and X-ray observations of clusters that agree with the same baryon fraction and with the predicted density profiles (e.g., Umetsu et al. 2018); the large-scale structure galaxy correlations (Alam et al. 2021); and the agreement with the baryon density inferred from primordial nucleosynthesis (Grohs & Fuller 2022).

Dark matter may be in the form of compact objects, which would be detectable through gravitational lensing. The baryon density derived from primordial nucleosynthesis and CMB observations rules out compact objects made of baryonic matter, but primordial black

holes (PBH) formed in the early universe from the collapse of the hot plasma in regions of large amplitude primordial perturbations can account for cold dark matter without requiring the addition of any particles to the Standard Model of particle physics (Hawking 1971). Although a number of astrophysical observations have constrained the contribution of PBH to the dark matter of the Universe (see Carr et al. 2021, for a review), the asteroid-mass window $10^{-16} M_{\odot} < m_b < 10^{-10} M_{\odot}$ remains completely open. Higher mass PBH are ruled out as constituents of all the dark matter by microlensing surveys in the Magellanic Clouds, although a small fraction of $\sim 10\%$ of dark matter in compact objects is still allowed (Alcock et al. 1998, 2001; Tisserand et al. 2007; Wyrzykowski et al. 2011a,b; Griest et al. 2014; Smyth et al. 2020).

Microlensing observations can provide independent constraints on the fraction of dark matter in compact objects from a different type of observations: highly magnified luminous stars lensed by clusters of galaxies that lie very near a lensing caustic. The high magnification allows a luminous star at a cosmological distance to be observed via our most powerful telescopes (Miralda-Escudé 1991). The presence of compact objects near the lensing critical line of the cluster replaces the smooth critical line with a corrugated network of micro-critical lines, and the higher the surface density of compact objects, the broader this network over which magnified images reaching the highest magnifications may be observed (Venumadhav et al. 2017; Oguri et al. 2018). The discovery of such highly magnified stars (Kelly et al. 2018) has opened the door to use these observations to constrain the presence of any compact objects in the dark matter of

★ miralda@icc.ub.edu

a lensing cluster (plus any dark matter along the line of sight contributing to the lensing deflection), which is over the contribution from intracluster stars that are known to be present.

In this paper we analyze the most interesting cases of highly magnified stars that have been reported in the literature to derive an upper limit to the fraction of dark matter in lensing clusters that may be in the form of dark, compact objects. Section 2 reviews the properties of the network of micro-critical lines that are relevant to derive this upper limit, and introduces an analytical approximation for the density of supermagnified images around this network. Our method to derive an upper limit on compact objects is described in Section 3, together with the list of supermagnified stars we use in this work. Our results are presented in Section 4, and we summarize our conclusion in Section 6.

2 THE DISTRIBUTION OF HIGHLY MAGNIFIED IMAGES AROUND THE SMOOTH CRITICAL LINE

We now discuss the expected distribution of highly magnified images in the observed image plane of a lens. If we imagine first a smooth lens, without any small-scale structure, highly magnified images are located in the vicinity of the critical lines (or lines where the determinant of the magnification matrix is zero), which are smooth curves. A real lensing cluster has some fraction of its mass in compact objects: at the very least, intracluster stars are present. The macro-model of the lens is defined to have the surface density resulting from smoothing the point masses over a scale that is much smaller than the total lens deflection but much larger than the separation among neighboring microlenses.

We follow [Venumadhav et al. \(2017\)](#), hereafter V17, to establish our nomenclature and notation. The macro-critical line (MaCL) is defined as the critical line of the lens macro-model. The true critical line takes into account the individual lensing stars in the intracluster light without smoothing, and is called the micro-critical line (MiCL). The MiCL is highly complex, with a corrugated band of angular width r_w where it meanders around many of the point masses. This angular width is given by (see eq. 22 in V17)

$$r_w = \frac{\kappa_\star}{g}, \quad (1)$$

where κ_\star is the contribution to the lensing convergence from the smoothed point masses, and g is the angular gradient modulus of the eigenvalue of the macro-model magnification matrix that vanishes at the MaCL (note that g is written as d in V17). In the region within a separation $r < r_w$ from the MaCL, the MiCLs are connected to each other and form an intricate, corrugated network that is affected everywhere by many point masses. Outside the corrugated network ($r > r_w$), the MiCLs are usually disconnected and form closed curves around each point mass, with the shape of the infinite symbol in the approximation of a single point mass with fixed external shear ([Chang & Refsdal 1979](#)).

We first review the analytical derivation for how the maximum magnification reached in MiCL crossings depends on r/r_w . The maximum magnification μ_p that is reached when a source star crosses a MiCL depends on the local eigenvalue gradient g_\star , computed including the point masses with no smoothing (whereas g is the eigenvalue gradient of the macro-lens model). We assume all microlenses have the same mass, corresponding to an Einstein radius θ_\star . The peak magnification is $\mu_p \propto (g_\star \sin \alpha_\star)^{-1/2}$ (eq. 27 in V17), where α_\star is the angle formed by the MiCL and the principal axis of the eigenvalue that cancels on the MiCL. The average separation between neighboring point masses is $\theta_\star/\kappa_\star^{1/2}$. Within the corrugated band, the MiCL

is a curve meandering around point masses at this typical separation, where the typical shear from point masses is $\lambda_\star \sim \kappa_\star$ and its gradient is $g_\star \sim \kappa_\star^{3/2}/\theta_\star$. Therefore, the distribution of peak magnifications of MiCL crossings is roughly constant within the width r_w , with the typical value scaling as $\mu_p \propto \theta_\star^{1/2} \kappa_\star^{-3/4}$. We assume that the distribution of the angle α_\star is random and independent of r , so it does not affect the proportionality relations we are discussing.

However, when moving outside the network at a separation $r > r_w$ from the MaCL, MiCLs are closed curves around individual point masses of a characteristic size $\theta_i \sim \theta_\star (\kappa_\star r/r_w)^{-1/2}$, where the characteristic shear is now $\lambda_\star \sim \kappa_\star (r/r_w)$ and the eigenvalue gradient is typically $g_\star \sim \lambda_\star/\theta_i \sim (\kappa_\star r/r_w)^{3/2}/\theta_\star$. The reason is that the shear of a point mass drops with the angular separation as θ_i^{-2} , and the shear from microlenses that needs to be added to the macro-model to reach a zero of the magnification eigenvalue increases as r/r_w . The peak magnification that is reached is therefore $\mu_p \propto \theta_\star^{1/2} (\kappa_\star r/r_w)^{-3/4}$. When expressed as a function of the source separation from the macroscopic caustic, $y \propto r^2$, the peak magnification drops as $\mu_p \propto y^{-3/8}$ outside the corrugated band of micro-caustics, and is flat inside (see eq. 27 in V17).

Nevertheless, what we actually want to infer here is not the dependence of peak magnifications on r , but the distribution of highly magnified images around the MaCL that reach a magnification above some threshold value, $\mu > \mu_t$. For this purpose, we compute first the fraction of the image plane area where the magnification is above μ_t , in the limit of high μ_t when this fraction is small, as a function of r . The region around each MiCL that has magnification $\mu > \mu_t$ has a width proportional to g_\star^{-1} , assuming the source star is small enough to be fully inside the corresponding width around the microcaustic in the source plane. Within $r < r_w$ this fraction is roughly constant because the distribution of g_\star is also roughly independent of r . Outside the corrugated band, the typical value of g_\star on MiCLs grows as $(r/r_w)^{3/2}$, and the length of MiCLs is proportional to their typical size around each point mass, or to $(r/r_w)^{-1/2}$. Therefore, the fraction of the area with $\mu > \mu_t$, scales as $g_\star^{-1} (r/r_w)^{-1/2} \sim (r/r_w)^{-2}$.

Because we have computed this area fraction at fixed μ , the density of micro-images above μ_t from sources that are randomly distributed in the source plane must also scale in the same way: roughly constant within r_w and falling as $(r/r_w)^{-2}$ at $r > r_w$. Based on these approximations, we adopt the following model for computing likelihood functions of the observed positions of highly magnified images:

$$p_i(r) dr = \frac{2}{\pi} \frac{dr/r_w}{1 + (r/r_w)^2}. \quad (2)$$

We note that this expression for the function $p_i(r)$ assumes that the source star is small enough not to have reached the maximum possible magnification, which is produced when the stellar disk lies on the micro-caustic. Once this maximum magnification is reached, the probability density p_i drops much faster with r than in equation (2), because most MiCL become too small to reach the required magnification.

3 CORRUGATED BAND WIDTHS

Our goal in this section is to measure the distribution of separations from the MaCL in a sample of supermagnified stars, to derive an upper limit on the surface density of microlenses. For this purpose, we select a list of 12 supermagnified star candidates that had been reported as this work was being done, listed in Table 1. The list starts with the initial discovery of Icarus ([Kelly et al. \(2018\)](#)), up to the recent report of Mothra ([Diego et al. \(2023a\)](#)).

We consider these events are most likely to be true supermagnified stars. Supermagnified stars will follow the distribution of equation (2) only when their detection requires a minimum magnification threshold to make them visible, and the source size is small enough to remain unresolved when magnified (otherwise the images will be considered as typical surface brightness irregularities that are seen in many lensed galaxies). Single star candidates may be confused with other objects, mainly compact globular clusters that remain unresolved, but this is unlikely for most of these candidates since clusters that are compact enough are rare (see Welch et al. 2022a). The main criteria to consider these events as good supermagnified star candidates are photometric data that are consistent with the spectra of some of the most luminous stars (generally supergiants or very massive main-sequence stars), and variability on timescales of \sim days that is consistent with being caused by MiCL crossings of sources with radii typical of the most luminous known stars, with a lack of observed counterimages which are typically not seen because of insufficient magnification.

These candidates generally satisfy these criteria. There are doubts, however, on the nature of the two Spock objects and Godzilla (events labeled as 2, 3 and 6 in Table 1), which may be more consistent with flaring luminous blue variables (similar to Eta Carinae) or recurrent novae (Rodney et al. 2018; Diego et al. 2022), especially in view of their high brightness. In addition, for these cases it is difficult to determine precisely where the MaCL lies (see in particular the discussion in Diego et al. 2022), and therefore the separation r from the observed variable images to the MaCL. The position of the MaCL can often be determined rather precisely when pairs of images of surface brightness irregularities can be identified, and the MaCL must lie in the middle of such pairs when the pairs are much closer together compared to the size of the MaCL. This generally gives a high confidence in the modelled separations r listed in column 9 of Table 1 for the remaining 9 cases, all of which have consistent photometry and variability to be microlensing events of single stars or compact systems of few stars (binaries or multiple hierarchical binaries).

For each of the events, we compute the convergence on the MaCL κ_0 , the eigenvalue inverse gradient g^{-1} , and the angular separation from the image to the MaCL r , using publicly available galaxy cluster lens models, such as the Hubble Frontier Fields (HFF) (Lotz et al. (2017)), CLASH (Postman et al. (2012)) or RELICS (Coe et al. (2019)) programs. For each model we use maps of the magnification matrix parameters, with the ratio of angular diameter distances D_{LS}/D_S rescaled to the source redshift to infer κ_0 and g^{-1} . We evaluate the eigenvalue gradient at the MaCL, $\mathbf{g} = -(\nabla\kappa)_0 - (\nabla\gamma)_0$, at the point of the model MaCL which is connected to the star image by a segment that is parallel to the principal axis of the vanishing eigenvalue (i.e., the direction of image elongation). The derivatives of the convergence and shear along this segment are evaluated by subtraction of the values at points separated by ~ 10 times the pixel size in each lens model sky map. The presented values of κ_0 and g^{-1} are obtained by averaging over the models listed in Table 1. Statistical dispersions are generally small ($\sim 2\%$ for κ_0 and $\sim 10\%$ for g^{-1}), with exception of cases 1 and 5, where they reach values of $\sim 10\%$ and $\sim 40\%$ for κ_0 and g^{-1} , respectively.

We list also the convergence contributed by stars that is implied by the intracluster light brightness near the image, κ_\star , that is reported in the listed references for 6 of the 9 events. In most cases, values of the surface mass density in microlenses (Σ_\star) is reported after assuming a Salpeter or Chabrier initial mass function, and we then compute $\kappa_\star = \Sigma_\star/\Sigma_{\text{crit}}$. This measurement of Σ_\star is not reported yet for the other 3 cases.

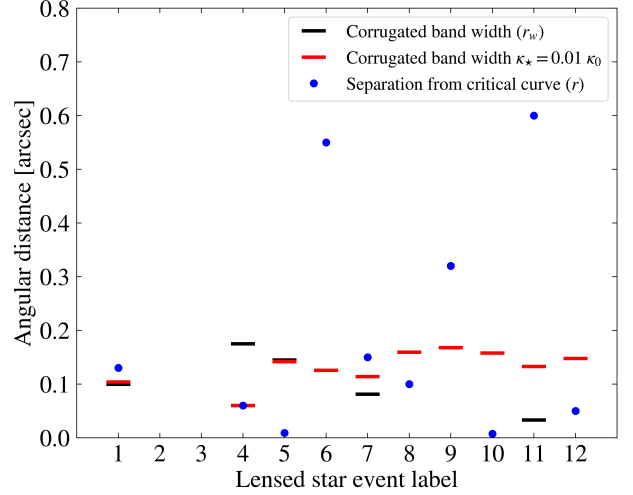


Figure 1. Angular distance r from each of the 12 highly magnified star images to the model macro critical line (MaCL) (blue dots), compared to the half-width of the corrugated band of micro-critical lines (r_w , black bars) when the surface density κ_\star is that corresponding to the intracluster light, and the same corrugated band half-width for $\kappa_\star = 0.01 \kappa_0$ (red bars). Events 2, 3 and 6 are excluded from our analysis because of uncertainties on the nature of the sources and the lens model of the MaCL.

The predicted corrugated band half widths, r_w , are then computed using equation (1), and are shown as black horizontal bars in Figure 1, for all the 9 events we use. For event number 6 we did not have the magnification matrix of the lens model available and the red bar indicates the mean of the other lenses.

We also show as red horizontal bars the same bandwidth r_w when we assume that compact objects account for 1% of the total mass surface density of the lensing model (i.e., $\kappa_\star = 0.01 \kappa_0$). The observed angular separations between the star images and each model MaCL are shown as blue dots.

We see that generally, the images are always observed at the expected separations from the MaCL, compared to r_w . There are two cases where the image is substantially further, events 6 and 11. As discussed earlier, we do not consider event 6 in view of the modeling uncertainties; in fact the large separation from the MaCL for this event is quite unreliable and may actually be much smaller, as discussed by Diego et al. (2022). However, we think that event 11, and also event 9 with a more moderate separation outside the corrugated band, are real cases of microlensed stars that can occur further from the MaCL according to equation (2), as we further discuss below.

4 RESULTS

We now proceed to a maximum likelihood estimate of the optimal value of κ_\star to explain the distribution of separations in Figure 1, and an upper limit to the fraction of dark matter that may be composed of compact objects. Initially, we assume for simplicity that any compact objects accounting for part of the dark matter have a similar mass distribution as the intracluster stars, and in the next section we discuss the range of masses that our limit actually applies to.

Using the probability density function $p_i(r)$ of equation (2), we define the likelihood function

$$\ln \mathcal{L}(\kappa_b) = \sum_i \ln p_i(\kappa_b), \quad (3)$$

where $p_i(r_i, g_i, \kappa_b)$ is the probability density of observing a stellar

Event label	Lens cluster	Star name	z_L	z_S	κ_0	g^{-1} [arcsec]	κ_\star	r [arcsec]	AB mag [mag]
1 ^a	MACS J1149	Icarus (Kelly et al. 2018)	0.54	1.49	0.832	12.46	0.0080	0.13	25-26 (F125W)
2 ^b	MACS J0416	Spock-NW (Rodney et al. 2018)	0.397	1.0054	0.742	10.29	0.0028	...	25-26.5 (F814W)
3 ^b	MACS J0416	Spock-SE (Rodney et al. 2018)	0.397	1.0054	0.629	10.29	0.0028	...	23-26.5 (F160W)
4 ^c	MACS J0416	Warhol (Kaurov et al. 2019)	0.397	0.94	0.686	8.74	0.02	0.06	26.25 (F125W)
5 ^d	WHL0137-08	Earendel (Welch et al. 2022a)	0.566	6.2	0.590	24.01	0.0060	0.009	27.2 (F150W)
6 ^e	PSZ1 G311.65	Godzilla (Diego et al. 2022)	0.443	2.37	0.55	≈ 22 (F814W)
7 ^f	Abell 2744	LS7 (Chen et al. 2022)	0.308	2.65	0.726	15.68	0.0052	0.15	27.05 (F150W)
8 ^g	MACS J0647	star-1 (Meena et al. 2023b)	0.591	4.8	0.544	29.28	...	0.1	27.343 (F227W)
9 ^g	MACS J0647	star-2 (Meena et al. 2023b)	0.591	4.8	0.549	30.59	...	0.32	28.330 (F227W)
10 ^h	El Gordo	Quyllur (Diego et al. 2023b)	0.870	2.1878	0.662	23.84	...	$7.5 \cdot 10^{-3}$	25.5 (F356W)
11 ⁱ	Abell 370	LS11 (Meena et al. 2023a)	0.375	1.2567	0.703	18.89	0.0017	0.6	29.51 (F200LP)
12 ^j	MACS J0416	Mothra (Diego et al. 2023a)	0.397	2.091	0.936	15.78	...	0.05	≈ 27.8 (F200W)

Table 1. List of 12 supermagnified star candidates, with lens and source redshifts z_L and z_S , convergence at image position κ_0 , eigenvalue inverse gradient $\mathbf{g} = \nabla(-\kappa - \gamma)$ at the macro critical curve (MaCL), angular separation from source to MaCL r , and observed AB magnitude of each transient at given filter (AB mag). The values of κ_0 and g^{-1} are the average of the set of publicly available lens models for each lens.

^a CATS (v4.1) (Richard et al. 2014), Zitrin-ltm (v1) (Zitrin et al. 2009; Zitrin et al. 2013), GLAFIC (v3) (Oguri 2010; Kawamata et al. 2016) and Keeton (v4) (McCully et al. 2014, Ammons et al. 2014, Keeton 2010)).

^b Williams (v4) (Sebesta et al. 2016, Liesenborgs et al. 2006) and Bradač (v3) (Hoag et al. 2016, Bradač et al. 2005, Bradač et al. 2009)).

^c Caminha (v4) (Caminha et al. 2017a), GLAFIC (v4) (Oguri 2010, Kawamata et al. 2016, Kawamata et al. 2018)), Keeton (v4) (McCully et al. 2014, Ammons et al. 2014, Keeton 2010)), Sharon (v4 Cor.) (Johnson et al. 2014, Jullo et al. 2007)), Zitrin-ltm-gauss (v3) and Zitrin-nfw (v3) (Zitrin et al. 2009, Zitrin et al. 2013)).

^d Zitrin-ltm (v1) (Zitrin et al. 2009, Zitrin et al. 2015)), GLAFIC (v1) (Oguri 2010)), WSLAP (v1) (Sendra et al. 2014) and Lenstool (v1) (Johnson et al. 2014, Jullo et al. 2007)).

^e No public lens models found.

^f Sharon (v4 Cor.) (Johnson et al. 2014, Jullo et al. 2007)).

^g Zitrin-ltm-gauss (v2) and Zitrin-nfw (v2) (Zitrin et al. 2009, Zitrin et al. 2013)).

^h Diego (v1) (Diego et al. 2023b)).

ⁱ GLAFIC (v4) (Oguri 2010, Kawamata et al. 2016, Kawamata et al. 2018)), Williams (v4) (Sebesta et al. 2019) and Keeton (v4) (McCully et al. 2014, Ammons et al. 2014, Keeton 2010)).

^j Zitrin-ltm-gauss (v3) (Zitrin et al. 2009, Zitrin et al. 2013)).

microlensing event at a distance r_i from the MaCL of event i , given a microlensing band of width $r_{w,i} = (\kappa_{\star,i} + \kappa_b)/g_i$. We are assuming that the total contribution from point masses to microlensing is the sum of the known intracluster light (κ_\star) and a hypothetical contribution from dark matter compact objects, such as primordial black holes (κ_b). We then find the optimal value of κ_b that maximizes this likelihood function.

The result for the likelihood function is shown in Figure 2. The optimal value of the dark matter surface density is $\kappa_b \approx 0.95 \times 10^{-3}$, and is consistent with zero. Therefore, the observed distribution of supermagnified star images is consistent with no compact objects in the dark matter, with the known stellar population in the intracluster light being ideal for explaining the observations. Figure 2 shows also the (1, 2, 3) σ upper limits that can be placed on any additional compact objects, if we treat the $\ln \mathcal{L}$ function as a χ^2 function. The 3 σ upper limit, at a confidence level of 0.3%, is $\kappa_b < 0.019$. We warn that this upper limit includes only the statistical uncertainty associated with the 9 events we used, but we have not attempted to incorporate other uncertainties due to the modeling of the lenses or the mass function of the stars in the intracluster light. These values for the upper limits to the fraction of dark matter in compact objects should also be slightly increased when we take into account that $\sim 10\%$ of the total mass contributing to lensing is in the hot, X-ray emitting gas (note that the gas usually has a density profile that is less centrally concentrated than the dark matter in the strong lensing region).

As discussed at the beginning of Section 3, we have excluded from this analysis event 6, which similarly to event 11 has a magnified

image further from the model MaCL by a factor ~ 4 than the predicted width r_w for $\kappa_\star = 0.01\kappa_0$, because of the model uncertainty in the true separation from the MaCL. Had we included this event, the 3 σ upper limit on κ_b increases only to $\kappa_b < 0.022$.

As a consequence, we can establish an upper limit to the fraction of dark matter that may be in compact objects. The average local convergence in the 9 events we have used is $\bar{\kappa}_0 = 0.691$, so the 3 σ upper limit on the dark matter fraction in compact objects is $\kappa_b/\bar{\kappa}_0 \approx 2.8\%$, which is only slightly increased to $\approx 3\%$ when taking into account the contribution of hot gas to $\bar{\kappa}_0$.

5 DEPENDENCE ON THE MICROLENS MASS DISTRIBUTION

The upper limit derived in this paper on the contribution of compact objects to the dark matter actually extends over a very broad mass range. A remarkable result of the microlensing effect of compact masses is that the width of the corrugated network of MiCLs is simply $r_w = \kappa_\star/g$, and is independent of the mass distribution of the microlenses. The mass of the microlenses affects only the maximum magnification and frequency of the MiCL crossing events.

Let us first consider the case of compact objects in the dark matter that are much more massive than stars, with Einstein radius and convergence θ_b and κ_b . These compact objects should produce their own network of MiCLs, and the intracluster stars should produce a second level of corrugation on a smaller scale, corresponding to their smaller Einstein radius. Without the intracluster stars, the peak

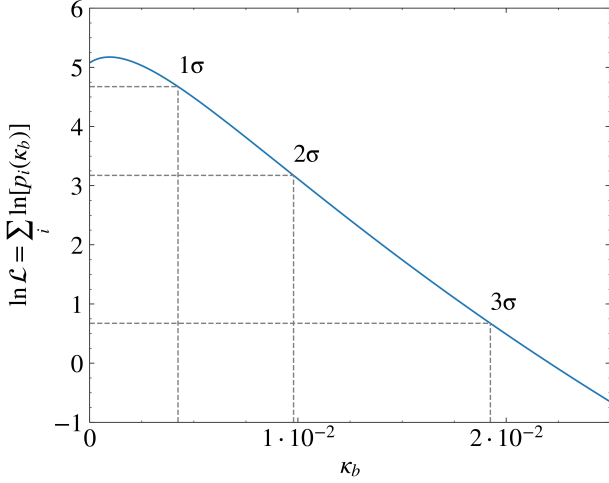


Figure 2. Likelihood function $\ln \mathcal{L}$ as a function of the convergence contributed by compact objects in the dark matter, κ_b , which may be primordial black holes or other dark matter compact objects but does not include the known contribution from intracluster stars.

magnification of MiCL crossings within the network is typically (equations 20 and 27 of [Venumadhav et al. 2017](#))

$$\mu_{pb} \approx \frac{1}{|1 - \kappa_0|} \left(\frac{D_S \theta_b}{R} \right)^{1/2} \kappa_b^{-3/4}, \quad (4)$$

where R is the radius of the source star. We note that this peak magnification does not actually depend on the gradient g , but only on θ_b and κ_b . Below a critical convergence $\kappa_{c1} = (g\theta_b)^{2/3}$, there is no corrugated network. When the intracluster stars are added, a second level of corrugation appears on the MiCLs caused by the more massive dark matter compact objects, with an external eigenvalue gradient $g_b \sim \kappa_b^{3/2}/\theta_b$ (equation 26 in [Venumadhav et al. 2017](#)), if κ_\star is greater than a new critical convergence, $\kappa_{c2} = (g_b \theta_\star)^{2/3} = \kappa_b (\theta_\star/\theta_b)^{2/3}$. The condition $\kappa_\star > \kappa_{c2}$ for the second level of corrugation to appear is the same as requiring that $\theta_\star^{1/2}/\kappa_\star^{3/4} < \theta_b^{1/2}/\kappa_b^{3/4}$. In other words, it is the same condition as requiring that stars dominate the impact on the peak magnification, which is given by

$$\mu_{p\star} \approx \frac{1}{|1 - \kappa_0|} \left(\frac{D_S \theta_\star}{R} \right)^{1/2} \kappa_\star^{-3/4}. \quad (5)$$

If $\kappa_\star < \kappa_{c2}$, then the second level of corrugation is not formed, and the peak magnification is limited by the presence of the dark matter compact objects instead of the stars, according to equation (4).

In any case, we note that any restrictions that can be inferred from the maximum magnification that can be reached in MiCL crossings to allow the detection of a star, once a maximum intrinsic luminosity of the source star is assumed, are *in addition* to the restriction that the supermagnified images should be uniformly distributed around the MaCL within the width r_w determined by the total surface density in compact objects. The first limits on κ_b were obtained by [Oguri et al. \(2018\)](#), but they were based on requiring that the maximum magnification of MiCL crossings was sufficient to explain the observed flux given a maximum luminosity assumed for the source star. This limit may be subject to uncertainties arising from the possible presence of a high-magnification tail due, for example, to rare cusps on the MiCLs, and is completely independent from the limit on κ_b we study here using the distribution of magnified images around the

MaCL. In our case, the important fact is that images reaching the peak magnification of equation (5) or (4), whichever is *lower*, should be uniformly distributed within the width r_w determined by the *total* surface density in compact objects of masses comparable or higher than stars.

Hence, our limit implies that no more than $\sim 3\%$ of the dark matter can be in any compact objects above stellar masses, up to a maximum mass at which $\kappa_b = \kappa_{cb} = (g\theta_b)^{2/3}$. For the upper limit $\kappa_b < 0.02$, and the median value of the eigenvalue gradient for our cluster lenses $g^{-1} \approx 16$ arcsec, this corresponds to $\theta_b \sim 0.05$ arcsec, or masses of 10^9 to $10^{10} M_\odot$. Above this mass, the dark matter compact objects with $\kappa_b = 0.02$ would produce isolated perturbations to the MaCL that could be individually identified around each object, which would stand out as a measurable perturbation caused by a dark object that is not associated with any luminous galaxy. Therefore, they would also be detectable in any case through their noticeable effect on cluster lensing models, above a minimum abundance that would need to be studied in more detail but which is unlikely to be close to the κ_{cb} threshold for corrugation.

Our limit actually applies also to extended lenses that may be subcritical to lensing on their own, but become supercritical close to the cluster MaCL, such as dark matter subhalos. We note that cluster galaxies may well exceed a contribution of 2% to the mass surface density, and their effects are in fact often visible on the shape of critical lines when they pass close to their vicinity, but this is taken into account in the lensing models with the identified luminous cluster galaxies. Similarly, if dark matter subhalos that are sufficiently dense exceed this upper limit of $\sim 2\%$ to their surface density contribution, they would have an important effect widening the region of maximally magnified images around the MaCL (see [Dai et al. 2018](#)), although some low-mass subhalos might remain subcritical to lensing even closer to the MaCL, and might then exceed this contribution without being easily detectable.

Next, we discuss the case of dark matter compact objects that are much less massive than stars. Exactly as in the previous case, the maximum magnification that will be reached in MiCL crossings will now be reduced to the value given in equation (4), where now $\theta_b < \theta_\star$, provided that $\kappa_b > \kappa_\star (\theta_b/\theta_\star)^{2/3}$. Otherwise, the peak magnifications will be the same as those caused by the intracluster stars alone. The total width of the corrugated network depends only on the total surface density of compact objects contributing to the two levels of corrugation.

However, there is in this case a different limitation to the detection of the microlensing effect: for any fixed κ_b , in the limit of very small masses of dark matter compact objects, the case of smooth dark matter must obviously be recovered. If the crossings of MiCLs can be detected down to a photometric accuracy of a fraction f of the total flux, then the peak magnification of equation (4) must exceed $f\mu(r)$, where the mean magnification at angular separation r from the MaCL is $\mu(r) \approx |1 - \kappa_0|^{-1}/(rg|\sin \alpha|)$ (equation 10 in [Venumadhav et al. 2017](#)), and α is the angle between the MaCL and the principal axis of the vanishing eigenvalue. Applying this to the typical separation where most highly magnified images should be seen, $r \sim r_w = (\kappa_b + \kappa_\star)/g$, we obtain the condition

$$\theta_b > \frac{R}{D_S} \frac{f^2 \kappa_b^{3/2}}{(\kappa_\star + \kappa_b)^2 |\sin \alpha|^2}. \quad (6)$$

For the case $\kappa_b \sim \kappa_\star \sim 0.01$, and $|\sin \alpha| \approx 1/2$ and $f \sim 1/2$, we find that $D_S \theta_b/R \gtrsim 2.5$, and for a typical stellar size and source angular diameter distance $R/D_S \sim 10^{-15}$, we find $\theta_b \gtrsim 5 \times 10^{-10}$ arcsec, implying that masses down to $10^{-6} M_\odot$ are still ruled out to contribute a surface density greater than $\kappa_b \gtrsim 0.02$ because any highly

magnified, variable images would be observed over a width larger than observed around the MaCL.

Note that for the microlensing mass that produces a typical magnification peak equal to the average magnification (i.e., when equation (6) is an equality with $f = 1$), this peak magnification is

$$\mu_{pb} = \frac{1}{|(1 - \kappa_0) \sin \alpha|(\kappa_\star + \kappa_b)}, \quad (7)$$

as expected at the separation $\sim r_w$ from the MaCL.

6 CONCLUSIONS

The result presented in this paper implies that the observation of only 9 supermagnified stars in lensing clusters of galaxies places an upper limit of 3% on the fraction of dark matter in compact objects which is already better than upper limits obtained so far from several microlensing surveys that have monitored millions of stars in the Magellanic Clouds (Alcock et al. 2001; Tisserand et al. 2007; Wyrzykowski et al. 2011b). Models of primordial black holes making up the dark matter are now ruled out for masses $m_b \gtrsim 10^{-6} M_\odot$ for fractions higher than $\sim 3\%$ at the 99% confidence level. Interestingly, this limit is sensitive to the dark matter that is present in the most massive clusters of galaxies in the Universe, and also to the intergalactic dark matter that must be present along the line of sight to the source that traverses the lensing cluster and contributes to the total lensing convergence.

As the observations of variability in lensing clusters improve in the future with further observations of JWST and other telescopes, we can look forward to an improvement in these limits, and also to new constraints on the mass function of the microlenses caused by intra-cluster stars, or perhaps other unknown objects. Other models such as the QCD axion, which predicts the presence of axion minihalos that can also have lensing effects despite their extended mass distribution (Dai & Miralda-Escudé 2020), will likely be constrained as well by monitoring campaigns of the supermagnified stars discovered by Kelly et al. (2018)

7 ACKNOWLEDGMENTS

This work has used gravitational lensing models produced by PIs Bradač, Natarajan and Kneib (CATS), Merten and Zitrin, Sharon, Williams, Keeton, Bernstein and Diego, and the GLAFIC group. This lens modeling was partially funded by the HST Frontier Fields program conducted by STScI. STScI is operated by the Association of Universities for Research in Astronomy, Inc. under NASA contract NAS 5-26555. The lens models were obtained from the Mikulski Archive for Space Telescopes (MAST). This work is also based on observations taken by the RELICS Treasury Program (GO 14096) with the NASA/ESA HST, which is operated by the Association of Universities for Research in Astronomy, Inc., under NASA contract NAS5-26555. This work was supported in part by Spanish grants PID2019-108122GB-C32 and PID2022-137268NB-C52.

8 DATA AVAILABILITY

The data and code used for the work presented in this article are available at <https://doi.org/10.6084/m9.figshare.25438648.v1>.

REFERENCES

- Alam S., et al., 2021, *Phys. Rev. D*, **103**, 083533
 Alcock C., et al., 1998, *ApJ*, **499**, L9
 Alcock C., et al., 2001, *ApJ*, **550**, L169
 Ammons S. M., Wong K. C., Zabludoff A. I., Keeton C. R., 2014, *ApJ*, **781**, 2
 Balestra I., et al., 2016, *ApJS*, **224**, 33
 Bradač M., Schneider P., Lombardi M., Erben T., 2005, *A&A*, **437**, 39
 Bradač M., et al., 2009, *ApJ*, **706**, 1201
 Caminha G. B., et al., 2017a, *A&A*, **600**, A90
 Caminha G. B., et al., 2017b, *A&A*, **600**, A90
 Carr B., Kohri K., Sendouda Y., Yokoyama J., 2021, *Reports on Progress in Physics*, **84**, 116902
 Castellano M., et al., 2016, *A&A*, **590**, A31
 Cerny C., et al., 2018, *ApJ*, **859**, 159
 Chan B. M. Y., Broadhurst T., Lim J., Diego J. M., Zitrin A., Coe D., Ford H. C., 2017, *ApJ*, **835**, 44
 Chang K., Refsdal S., 1979, *Nature*, **282**, 561
 Chen W., et al., 2019, *ApJ*, **881**, 8
 Chen W., et al., 2022, *ApJ*, **940**, L54
 Christensen L., et al., 2012, *MNRAS*, **427**, 1953
 Coe D., Bradley L., Zitrin A., 2015, *ApJ*, **800**, 84
 Coe D., et al., 2019, *ApJ*, **884**, 85
 Cypriano E. S., Sodr e Laerte J., Kneib J.-P., Campusano L. E., 2004, *ApJ*, **613**, 95
 Dai L., Miralda-Escud e J., 2020, *AJ*, **159**, 49
 Dai L., Venumadhav T., Kaurov A. A., Miralda-Escud e J., 2018, *ApJ*, **867**, 24
 Diego J. M., Broadhurst T., Molnar S. M., Lam D., Lim J., 2015, *MNRAS*, **447**, 3130
 Diego J. M., Pascale M., Kavanagh B. J., Kelly P., Dai L., Frye B., Broadhurst T., 2022, *A&A*, **665**, A134
 Diego J. M., et al., 2023a, *arXiv e-prints*, p. arXiv:2307.10363
 Diego J. M., et al., 2023b, *A&A*, **672**, A3
 Ebeling H., Barrett E., Donovan D., Ma C. J., Edge A. C., van Speybroeck L., 2007, *ApJ*, **661**, L33
 Ebeling H., Ma C.-J., Barrett E., 2014, *ApJS*, **211**, 21
 Einasto J., Kaasik A., Saar E., 1974, *Nature*, **250**, 309
 Griest K., Cieplak A. M., Lehner M. J., 2014, *ApJ*, **786**, 158
 Grillo C., et al., 2015, *ApJ*, **800**, 38
 Grohs E., Fuller G. M., 2022, in , *Handbook of Nuclear Physics*. p. 127, doi:10.1007/978-981-15-8818-1_127-1
 Hawking S., 1971, *MNRAS*, **152**, 75
 Hoag A., et al., 2016, *ApJ*, **831**, 182
 Jauzac M., et al., 2014, *MNRAS*, **443**, 1549
 Johnson T. L., Sharon K., Bayliss M. B., Gladders M. D., Coe D., Ebeling H., 2014, *ApJ*, **797**, 48
 Jullo E., Kneib J. P., Limousin M., El afsd ottir  ., Marshall P. J., Verdugo T., 2007, *New Journal of Physics*, **9**, 447
 Kaurov A. A., Dai L., Venumadhav T., Miralda-Escud e J., Frye B., 2019, *ApJ*, **880**, 58
 Kawamata R., Oguri M., Ishigaki M., Shimasaku K., Ouchi M., 2016, *ApJ*, **819**, 114
 Kawamata R., Ishigaki M., Shimasaku K., Oguri M., Ouchi M., Tanigawa S., 2018, *ApJ*, **855**, 4
 Keeton C. R., 2010, *General Relativity and Gravitation*, **42**, 2151
 Kelly P. L., et al., 2018, *Nature Astronomy*, **2**, 334
 Lagattuta D. J., et al., 2017, *MNRAS*, **469**, 3946
 Liesenborgs J., De Rijcke S., Dejonghe H., 2006, *MNRAS*, **367**, 1209
 Lotz J. M., et al., 2017, *ApJ*, **837**, 97
 Madhavacheril M. S., et al., 2023, *arXiv e-prints*, p. arXiv:2304.05203
 Mahler G., et al., 2018a, *MNRAS*, **473**, 663
 Mahler G., et al., 2018b, *MNRAS*, **473**, 663
 Mann A. W., Ebeling H., 2012, *MNRAS*, **420**, 2120
 McCully C., Keeton C. R., Wong K. C., Zabludoff A. I., 2014, *MNRAS*, **443**, 3631
 Meena A. K., et al., 2023a, *MNRAS*, **521**, 5224

- Meena A. K., et al., 2023b, *ApJ*, 944, L6
- Merlin E., et al., 2015, *A&A*, 582, A15
- Merlin E., et al., 2016, *A&A*, 590, A30
- Merten J., et al., 2011, *MNRAS*, 417, 333
- Miralda-Escudé J., 1991, *ApJ*, 379, 94
- Oguri M., 2010, *PASJ*, 62, 1017
- Oguri M., Diego J. M., Kaiser N., Kelly P. L., Broadhurst T., 2018, *Phys. Rev. D*, 97, 023518
- Okabe N., Umetsu K., 2008, *PASJ*, 60, 345
- Okabe N., Takada M., Umetsu K., Futamase T., Smith G. P., 2010a, *PASJ*, 62, 811
- Okabe N., Okura Y., Futamase T., 2010b, *ApJ*, 713, 291
- Ostriker J. P., Peebles P. J. E., Yahil A., 1974, *ApJ*, 193, L1
- Peebles P. J. E., 1982, *ApJ*, 263, L1
- Planck Collaboration et al., 2020, *A&A*, 641, A6
- Postman M., et al., 2012, *ApJS*, 199, 25
- Richard J., Kneib J. P., Limousin M., Edge A., Jullo E., 2010, *MNRAS*, 402, L44
- Richard J., et al., 2014, *MNRAS*, 444, 268
- Rodney S. A., et al., 2018, *Nature Astronomy*, 2, 324
- Rubin V. C., Ford W. K. J., Thonnard N., 1978, *ApJ*, 225, L107
- Salmon B., et al., 2020, *ApJ*, 889, 189
- Sebesta K., Williams L. L. R., Mohammed I., Saha P., Liesenborgs J., 2016, *MNRAS*, 461, 2126
- Sebesta K., Williams L. L. R., Liesenborgs J., Medezinski E., Okabe N., 2019, *MNRAS*, 488, 3251
- Sendra I., Diego J. M., Broadhurst T., Lazkoz R., 2014, *MNRAS*, 437, 2642
- Smith G. P., et al., 2009, *ApJ*, 707, L163
- Smyth N., Profumo S., English S., Jeltema T., McKinnon K., Guhathakurta P., 2020, *Phys. Rev. D*, 101, 063005
- Tisserand P., et al., 2007, *A&A*, 469, 387
- Treu T., et al., 2016, *ApJ*, 817, 60
- Tristram M., et al., 2024, *A&A*, 682, A37
- Umetsu K., Broadhurst T., Zitrin A., Medezinski E., Hsu L.-Y., 2011, *ApJ*, 729, 127
- Umetsu K., et al., 2018, *ApJ*, 860, 104
- Venumadhav T., Dai L., Miralda-Escudé J., 2017, *ApJ*, 850, 49
- Welch B., et al., 2022a, *Nature*, 603, 815
- Welch B., et al., 2022b, *ApJ*, 940, L1
- Wyrzykowski L., et al., 2011a, *MNRAS*, 413, 493
- Wyrzykowski L., et al., 2011b, *MNRAS*, 416, 2949
- Zheng W., et al., 2012, *Nature*, 489, 406
- Zitrin A., Broadhurst T., 2009, *ApJ*, 703, L132
- Zitrin A., et al., 2009, *MNRAS*, 396, 1985
- Zitrin A., et al., 2013, *ApJ*, 762, L30
- Zitrin A., et al., 2015, *ApJ*, 801, 44
- Zwicky F., 1933, *Helvetica Physica Acta*, 6, 110

This paper has been typeset from a $\text{\TeX}/\text{\LaTeX}$ file prepared by the author.